Generalized hyperboloid structures of polarization singularities in Laguerre-Gaussian vector fields

T. H. Lu, Y. F. Chen,* and K. F. Huang
Department of Electrophysics, National Chiao Tung University, Hsinchu, Taiwan 30050
(Received 10 August 2007; published 12 December 2007)

We present the propagation-dependent polarization vector fields by use of an isotropic microchip laser with the longitudinal-transverse coupling and the entanglement of the polarization states. With the coherent superposition of orthogonal circularly polarized vortex modes which are made up of two Laguerre-Gaussian modes with different order, the experimental three-dimensional vector fields can be reconstructed analytically. From the theoretical analyses, the generalized structures of singularities such as *V* points, *C* lines, and *L* surfaces can be clearly demonstrated. Importantly, the projections of *C* lines on the transverse plane are found to form the intriguing petal structures.

DOI: 10.1103/PhysRevA.76.063809 PACS number(s): 42.25.Ja, 02.40.Xx, 03.65.Vf, 42.60.Jf

I. INTRODUCTION

Singular optics which includes phase and polarization singularities has become an important topic in modern physics to understand the physics of light [1,2]. Recently, a considerable number of studies have been focused on experimental and theoretical results of phase singularities in scalar fields, known as wave front dislocations, such as optical vortices [3], vortex lattices in superconductors [4], quantum and microwave billiards [5], quantum Hall effects [6], and linear and nonlinear optics [7–9]. In addition to phase singularities in scalar fields, there are two types of polarization singularities in vector fields of paraxial optical beams, known as wave front disclinations, to be discussed: Vector singularities and Stokes singularities [10]. Vector singularities (*V* points) are stationary points at which the orientation of the electric vector of a linearly polarized vector field becomes undefined. The importance of the vector singularities has been explored in the optical coherent waves with the representation of spatial structures and polarization states [11–14]. Recently, the complicated *V* point structure has been studied from the low-order [15] and high-order [16] space-dependent linearly polarized fields in transversely isotropic laser systems. However, the mapping of vector field singularities onto the scalar field vortices leads to many new consequences [10].

The more general state of optical field with two orthogonal components is elliptically polarized state which leads to two special conditions of Stokes singularities: *C* lines, on which the field is circularly polarized and the orientations of the major and minor axes of the ellipse are undefined, and *L* surfaces, on which the field is linearly polarized and the handedness of the ellipse are undefined [17]. In paraxial optics, *C* lines present as isolated points in the observation plane and *L* surfaces present as continuous lines, *L* lines, which separate regions of right-handed and left-handed polarization [18–20]. With the experimental results of microwaves [10] and optical waves [21–24], the importance of polarization singularities of elliptically polarized fields has been revealed.

Recently, a diode-pumped microchip laser has been employed to generate the propagation-dependent polarization vector fields with the longitudinal-transverse coupling and the entanglement of the polarization states [25]. However, the characteristics of polarization singularities are revealed with the theoretical wave representation only in the condition of single-ring wave pattern. In this work, we demonstrate the general expression of the multiple structures of polarization singularities embedded in the multiring vector wave patterns. With the coherent superposition of orthogonal circularly polarized vortex modes composed of two Laguerre-Gaussian (LG) modes with different order, the general structures of the polarization singularities are systematically analyzed. The theoretical analyses reveal that the projection of the *C* lines on the transverse plane displays the intriguing petal structures. From the analytical results of the singularities, the polarization states of the experimental LG vector fields under propagation can be clearly demonstrated.

II. EXPERIMENTAL SETUP AND RESULTS

In this experiment, the laser system was a diode-pumped $Nd:YVO_4$ microchip laser and the resonator was formed by a spherical mirror and a gain medium. The spherical mirror was a 10 mm radius-of-curvature concave mirror with antireflection coating at the pumping wavelength on the entrance face ($R<0.2\%$), high-reflection coating at lasing wavelength ($R>99.8\%$), and high-transmission coating at the pumping wavelength on the other surface ($T>95\%$). The gain medium was a 2.0 at. % $Nd:YVO_4$ crystal with the length of 2 mm. The laser crystal was precisely cut along the *c* axis for high-level transverse isotropy [26]. One planar surface of the laser crystal was coated for antireflection at the pumping and lasing wavelengths; the other surface was coated to be an output coupler with the reflectivity of 99%. The pump source was a 1 W 808 nm fiber-coupled laser diode with a core diameter of 100 μm and a numerical aperture of 0.2. A focusing lens was used to reimage the pump beam into the laser crystal. The pump spot radius was controlled to be in the range 50–200 μm. The effective cavity length was set in the range 9.6–9.9 mm to form a nearly

*FAX: (886-35) 725230; yfchen@cc.nctu.edu.tw

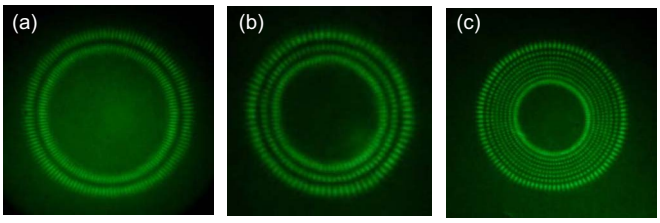

FIG. 1. (Color online) Experimental far-field transverse patterns with different radial index p and azimuthal index l: (a) $(p,l)=(1,66)$; (b) $(p,l)=(2,41)$; (c) $(p,l)=(7,100)$.

hemispherical resonator, in which the fundamental cavity mode size was approximately 20 μm. Since the pump-to-mode size ratio was significantly greater than unity, a variety of high-order transverse modes could be generated.

The pump power was controlled to be near lasing threshold to maintain the single mode in the cavity to explore the characteristic of polarization. To measure the far-field pattern, the output beam was directly projected on a paper screen at a distance of ~50 cm from the rear cavity mirror and the scattered light was captured by a digital camera. Figures 1(a)–1(c) show three experimental far-field transverse patterns which are represented as flower modes with different transverse radial index. Not only the single-ring but also the multiring is the general transverse mode formed by the propagation-dependent polarization states to prevail in the laser cavity. The fundamental mode is not excited because the pump-to-mode size ratio is significantly greater than unity and then the lasing threshold of fundamental mode is higher than that of high-order transverse modes. A microscope objective lens mounted on a translation stage was used to reimage the tomographic transverse patterns at different propagation position onto a CCD camera. Figure 2 displays the polarization-resolved transverse patterns at three different propagation positions: $z=0$, $z=z_R$, and $z\gg z_R$, where the Z_R is the Rayleigh range and $Z_R=1.28$ mm. It can be found that the polarization-resolved patterns represent as an azimuthally polarized flower mode at the beam waist ($z=0$), whereas it turns out to be like a radially polarized flower mode at the far field ($z\gg z_R$). Moreover, the polarization state at $z=z_R$ was confirmed to behave as a circularly polarized flower mode by use of a quarter-wave plate. The polarization-resolved transverse modes formed by the three-dimensional (3D) coherent vector field provide an important aspect to explore the physics of polarization singularities. It is worthwhile to mention that the lasing modes are propagation-dependent polarization vector fields which are generated from the nearly hemispherical cavity. The following analysis will substantiate that the longitudinal-transverse coupling with the entanglement of the polarization states leads to the formation of 3D coherent vector fields in the isotropic laser cavity. Therefore, the generalized structures of polarization singularities in coherent vector fields with longitudinal-transverse coupling can be clearly revealed with the theoretical analysis.

III. ANALYTICAL WAVE FUNCTIONS FOR EXPERIMENTAL PATTERNS AND POLARIZATION SINGULARITIES

According to the lasing modes represented as flower modes in the transverse patterns, we start from the LG mode to be the basis of the experimental results. The wave function of LG mode with longitudinal index s, transverse radial index p, and transverse azimuthal index l in cylindrical coordinates (ρ,ϕ,z) is given by $\Psi_{p,l,s}(\rho,\phi,z)=e^{il\phi}\Phi_{p,l,s}(\rho,z)$, where

$$\Phi_{p,l,s}(\rho,z)=\sqrt{\frac{2p!}{\pi(p+|l|)!}}\frac{1}{w(z)}\left(\frac{\sqrt{2}\rho}{w(z)}\right)^{|l|}L_p^{|l|}\left(\frac{2\rho^2}{w(z)^2}\right)\times\exp\left[-\frac{\rho^2}{w(z)^2}\right]\exp\left\{-ik_{p,l,s}z\left[1+\frac{\rho^2}{2(z^2+z_R^2)}\right]\right\}\times\exp[i(2p+|l|+1)\theta_G(z)] \quad (1)$$

where $w(z)=w_0\sqrt{1+(z/z_R)^2}$, w_0 is the beam radius at the waist, $z_R=\pi w_0^2/\lambda$ is the Rayleigh range, $L_p^l(\cdot)$ are the associated Laguerre polynomials, $k_{p,l,s}$ is the wave number, and $\theta_G(z)=\tan^{-1}(z/z_R)$ is the Gouy phase. In the resonator with the effective length L, the wave number $k_{p,l,s}$ is given by $k_{p,l,s}L=\pi[s+(2p+|l|)(\Delta f_T/\Delta f_L)]$, where $\Delta f_L=c/2L$ is the

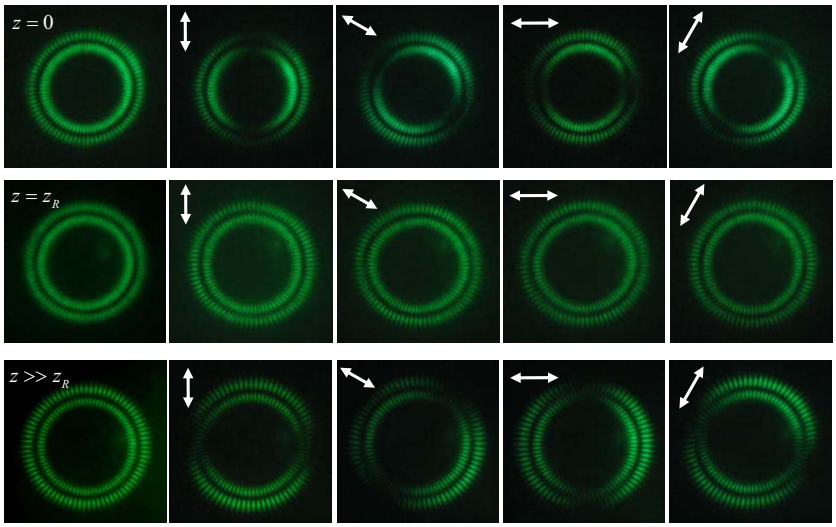

FIG. 2. (Color online) Polarization-resolved transverse patterns for the experimental result with the index $(p,l)=(1,39)$ at three different propagation positions: $z=0$, $z=z_R$, and $z\gg z_R$, where z_R is the Rayleigh range. The arrows indicate the transmission axis of the polarizer.

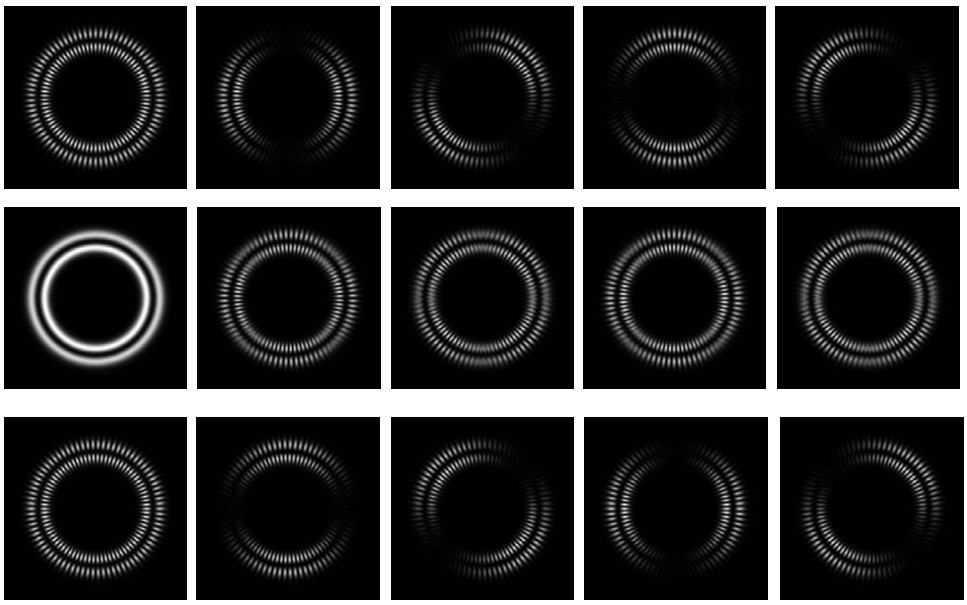

FIG. 3. Numerically reconstructed patterns for the experimental results shown in Fig. 2.

longitudinal mode spacing and Δf_T is the transverse mode spacing. It has been verified [27] that the longitudinal-transverse coupling and mode-locking effect can lead to the frequency locking among different transverse modes with the help of different longitudinal orders when the ratio $\Delta f_T/\Delta f_L$ is close to a simple fractional. As a result, the configuration of the nearly hemispherical cavity refers to be $\Delta f_T/\Delta f_L \approx 1/2$, and the group of LG modes $\Psi_{p,l+2k,s-k}(\rho,\phi,z)$, with $k=0,1,2,3\ldots$, forms an important family of frequency degenerate states. With LG modes as the basis, the experimental vector fields can be decomposed into a coherent superposition of orthogonal circularly polarized helical modes $\vec{E}=E_R(\rho,\phi,z)\hat{a}_R+E_L(\rho,\phi,z)\hat{a}_L$, where

$$E_R(\rho,\phi,z)=[\Psi_{p,-(l+1),s-1}(\rho,\phi,z)-\Psi_{p,l-1,s}(\rho,\phi,z)]/\sqrt{2}, \tag{2}$$

$$E_L(\rho,\phi,z)=[\Psi_{p,l+1,s-1}(\rho,\phi,z)-\Psi_{p,-(l-1),s}(\rho,\phi,z)]/\sqrt{2}, \tag{3}$$

and $\hat{a}_R=(\hat{a}_x-i\hat{a}_y)/\sqrt{2}$ and $\hat{a}_L=(\hat{a}_x+i\hat{a}_y)/\sqrt{2}$ are the helical basis unit vectors for the right- and left-handed circulation polarizations, respectively. Figure 3 displays the numerically reconstructed patterns for the experimental results shown in Fig. 2. There is a good agreement between the reconstructed and experimental patterns. From this point of view, the circularly polarized vortex modes indeed play an important role to form the propagation-dependent polarization vector fields. Equations (2) and (3) indicate that each circularly polarized component of the vector fields is composed of two LG modes with different order. It is worthwhile to mention that the frequency locking of two LG modes with different azimuthal orders arises from the longitudinal-transverse coupling in a nearly hemispherical cavity.

After some algebra, Eqs. (2) and (3) for the general condition can be simplified as

$$E_R(\rho,\phi,z)=[\tilde{\rho}_l^2 e^{-i2l\phi}e^{i2\theta_G(z)}-1]e^{i(l-1)\phi}\Phi_{p,l-1,s}(\rho,z)/\sqrt{2}, \tag{4}$$

$$E_L(\rho,\phi,z)=[\tilde{\rho}_l^2 e^{i2l\phi}e^{i2\theta_G(z)}-1]e^{-i(l-1)\phi}\Phi_{p,l-1,s}(\rho,z)/\sqrt{2}, \tag{5}$$

where

$$\tilde{\rho}_l^2=[\sqrt{2}\rho/w(z)]^2[1/\sqrt{(l+p)(l+p+1)}]\times\left[L_p^{l+1}\left(\frac{2\rho^2}{w(z)^2}\right)\Big/L_p^{l-1}\left(\frac{2\rho^2}{w(z)^2}\right)\right]. \tag{6}$$

In the basis of circular polarizations, the condition for left-handed and right-handed C point loci can be given by $E_R(\rho,\phi,z)=0$ and $E_L(\rho,\phi,z)=0$, respectively. For the paraxial 3D vector fields, the trajectories of C singularities can be expressed as the parametric curves with z as a variable. In addition to the central singularity at the origin, the expression in the bracket of Eq. (4) indicates the left-handed C point trajectories are determined by the following two conditions: (1) $\tilde{\rho}_l^2=1$ and $e^{-i2l\phi}e^{i2\theta_G(z)}=1$; (2) $\tilde{\rho}_l^2=-1$ and $e^{-i2l\phi}e^{i2\theta_G(z)}=-1$. In general, there are $2p+1$ solutions of the exact radius which the C points are symmetrically embedded in. Note that for $p=0$ there are $2l$ peripheral left-handed C points symmetrically arrayed on a circle of radius $\rho_0=\sqrt{\sqrt{l(l+1)}}w(z)/\sqrt{2}$ at angles $\phi_m=[\theta_G(z)+m\pi]/l$ with $m=0,1,2,\ldots,2l-1$ and $2l$ peripheral right-handed C points on the same circle of radius at angles $\phi_m=[-\theta_G(z)+m\pi]/l$ with $m=0,1,2,\ldots,2l-1$. The brief case of $p=0$ has been verified to be in good agreement with experimental results [25]. Besides $p=0$, the theoretical solution of radius with radial index p can be solved analytically for the cases $p=1-3$. Further, we analyzed the case of $p\geq 1$. For $p=1$, the three solutions of radius can be expressed analytically:

$$\rho_1 = \frac{1}{2}\sqrt{2 + l + \sqrt{(l+1)(l+2)} - \sqrt{6 + 7l + 2l^2 + 4\sqrt{(l+1)(l+2)} - 2l\sqrt{(l+1)(l+2)}}}w(z), \tag{7}$$

$$\rho_2 = \frac{1}{2}\sqrt{2 + l + \sqrt{(l+1)(l+2)} + \sqrt{6 + 7l + 2l^2 + 4\sqrt{(l+1)(l+2)} - 2l\sqrt{(l+1)(l+2)}}}w(z), \tag{8}$$

$$\rho_3 = \frac{1}{2}\sqrt{2 + l - \sqrt{(l+1)(l+2)} + \sqrt{6 + 7l + 2l^2 - 4\sqrt{(l+1)(l+2)} + 2l\sqrt{(l+1)(l+2)}}}w(z). \tag{9}$$

On the one hand, there are $2l$ peripheral left-handed and $2l$ peripheral right-handed C points symmetrically arrayed at angles $\phi_m=[\theta_G(z)+m\pi]/l$ and $\phi_m=[-\theta_G(z)+m\pi]/l$, respectively, with $m=0,1,2,\ldots,2l-1$ according to the circle radius in the situation of $\tilde{\rho}_l^2=1$, and, on the other hand, there are $2l$ peripheral left-handed and $2l$ peripheral right-handed C points symmetrically arrayed at angles $\phi_m=[2\theta_G(z)+(2m+1)\pi]/2l$ and $\phi_m=[-2\theta_G(z)+(2m+1)\pi]/2l$, respectively, with $m=0,1,2,\ldots,2l-1$ according to the circle radius in the situation of $\tilde{\rho}_l^2=-1$. As aresult, there are $2l(2p+1)$ left-handed C points and $2l(2p+1)$ right-handed C points embedded in the polarization-dependent vector field. Therefore, C lines singularities embedded in the propagation-dependent polarization vector field with $p=0$ form the hyperboloid structure. The theoretical results of the view from the propagation direction to the beam waist of the general structures of the C lines singularities with $p=1-3$ and $l=1-6$ are represented in Figs. 4–6. The different color of C line singularities represents the different allowable circle of radius according to the radial index p of the transverse modes. Therefore, the different radial position of the C line singularity with the same color implies the different propagation position of the propagation-dependent polarization vector field. The minimum of the radial position represents the beam waist and the maximum of the radial position represents the far field.

Another important and interesting feature is that the experimental 3D polarization vector fields at the beam waist and far field which are made up of two linearly polarized modes with different spatial structures. For the general condition, the experimental vector field can be given by $\vec{E}=E_x(\rho,\phi,p)\hat{x}+E_y(\rho,\phi,p)\hat{y}$, where

$$E_x(\rho,\phi,z) = \Phi_{p,l-1,s}(\rho,0)\{\tilde{\rho}_l^2 e^{i2\theta_G(z)}\cos[(l+1)\phi] - \cos[(l-1)\phi]\}\sqrt{2} \tag{10}$$

and

$$E_y(\rho,\phi,z) = \Phi_{p,l-1,s}(\rho,0)\{\tilde{\rho}_l^2 e^{i2\theta_G(z)}\sin[(l+1)\phi] + \sin[(l-1)\phi]\}/\sqrt{2}. \tag{11}$$

The transverse vector field at beam waist and far field can be verified to possess the V point singularities that are generally described in terms of the field of the angle function $\Theta(x,y)=\arctan(E_y/E_x)$ [10,28], where E_x and E_y are the scalar components of the vector field along the x and y axes. The vortices of $\Theta(x,y)$ are the vector singularities at which the orientation of the electric vector is undefined. Figures 7–9 show the angle pattern $\Theta(x,y)$ of the numerical vector field at the far field. Consistently, the V point singularities are right at

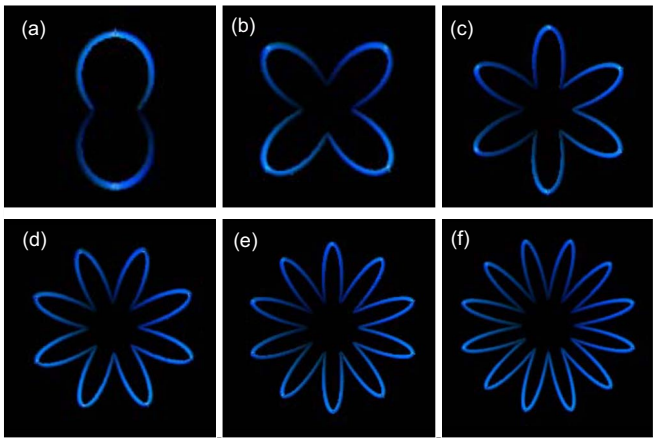

FIG. 4. (Color online) Structure of the C line singularities of the theoretical vector field from the view of propagation direction to the beam waist with the same radial index $p=0$ and different azimuthal index l: (a) $(p,l)=(0,1)$; (b) $(p,l)=(0,2)$; (c) $(p,l)=(0,3)$; (d) $(p,l)=(0,4)$; (e) $(p,l)=(0,5)$; (f) $(p,l)=(0,6)$.

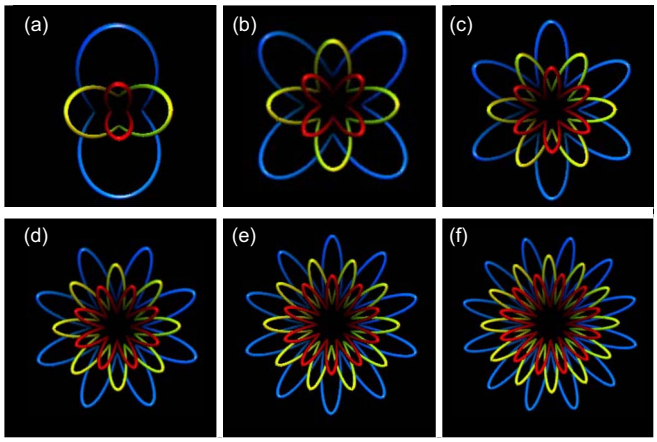

FIG. 5. (Color online) Structure of the C line singularities of the theoretical vector field from the view of propagation direction to the beam waist with the same radial index $p=1$ and different azimuthal index l: (a) $(p,l)=(1,1)$; (b) $(p,l)=(1,2)$; (c) $(p,l)=(1,3)$; (d) $(p,l)=(1,4)$; (e) $(p,l)=(1,5)$; (f) $(p,l)=(1,6)$.

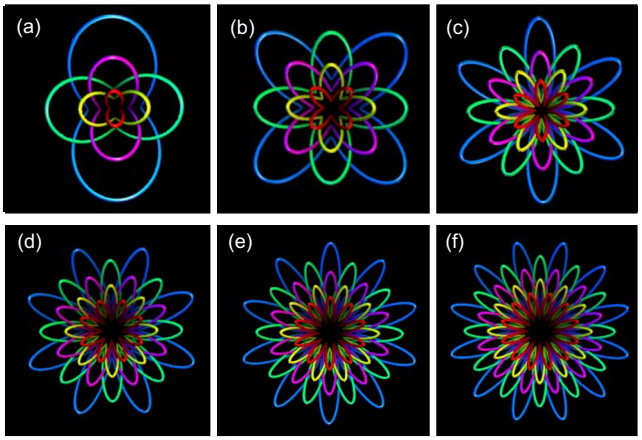

FIG. 6. (Color online) Structure of the C line singularities of the theoretical vector field from the view of propagation direction to the beam waist with the same radial index $p=2$ and different azimuthal index l: (a) $(p,l)=(2,1)$; (b) $(p,l)=(2,2)$; (c) $(p,l)=(2,3)$; (d) $(p,l)=(2,4)$; (e) $(p,l)=(2,5)$; (f) $(p,l)=(2,6)$.

the intersections of the right-handed and left-handed C lines shown in Fig. 4–6. With Eqs. (10) and (11) and some algebra, there are $2l$ peripheral V points symmetrically arrayed at angles $\phi_m=m\pi/l$ on a circle of radius ρ of the condition $\tilde{\rho}_l^2=1$ and $2l$ peripheral V points symmetrically arrayed at angles $\phi_m=(2m+1)\pi/2l$ on a circle of radius ρ of the condition $\tilde{\rho}_l^2=-1$ with $m=0,1,2,\ldots,2l-1$ at the beam waist in addition to the central singularity at the origin. The Gouy phase plays a vital role to transform the singularities between V points and C points under propagation of the 3D vector field. Consequently, there are $2l$ peripheral V points symmetrically arrayed at angles $\phi_m=(2m+1)\pi/2l$ on a circle of radius ρ of the condition $\tilde{\rho}_l^2=1$ and $2l$ peripheral V points symmetrically arrayed at angles $\phi_m=m\pi/l$ on a circle of radius ρ of the condition $\tilde{\rho}_l^2=-1$ with $m=0,1,2,\ldots,2l-1$ at the far field in addition to the central singularity at the origin. Intriguingly, each peripheral V point with the winding number of 1 is transformed to two different handed C points with

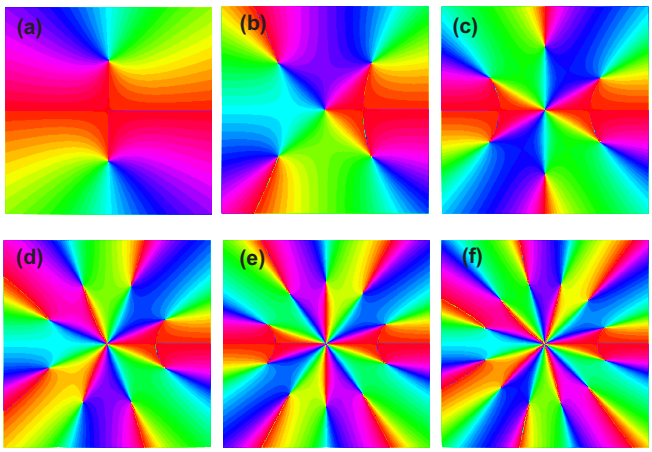

FIG. 7. (Color online) Numerical patterns of the angle function at the far field of the same radial index $p=0$ and different azimuthal index l: (a) $(p,l)=(0,1)$; (b) $(p,l)=(0,2)$; (c) $(p,l)=(0,3)$; (d) $(p,l)=(0,4)$; (e) $(p,l)=(0,5)$; (f) $(p,l)=(0,6)$.

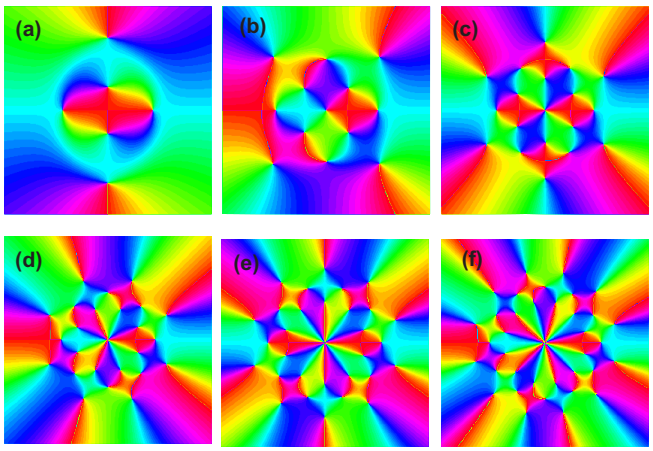

FIG. 8. (Color online) Numerical patterns of the angle function at the far field of the same radial index $p=1$ and different azimuthal index l: (a) $(p,l)=(1,1)$; (b) $(p,l)=(1,2)$; (c) $(p,l)=(1,3)$; (d) $(p,l)=(1,4)$; (e) $(p,l)=(1,5)$; (f) $(p,l)=(1,6)$.

the winding number of $1/2$. Apparently, the winding numbers are conserved during the singularity transformation and under the vector field propagation [29]. Figure 10 depicts the characteristics of the C line and V point singularities of an experimental result. It can be found that the structure of C lines shown in Fig. 10(b) forms the hyperboloid with multilayer in the radial direction. The theoretical pattern of the view from the propagation direction to the beam waist of the structures of the C lines singularities forms a kind of fascinating petal pattern corresponding to the experimental transverse pattern shown in Fig. 10(a).

Besides C line and V point singularities, there is L surface singularity embedded in the propagation-dependent polarization vector fields with the longitudinal-transverse coupling and the entanglement of the polarization states. The L singularities can be determined by the conditions $|E_R|^2=|E_L|^2$. With Eqs. (4) and (5), it can be found that there are $4l$ L surfaces on the ρ-z plane with the azimuthal angles at $\phi_n=n\pi/(2l)$, where $n=0,1,2,\ldots,4l-1$. Figure 11 displays the

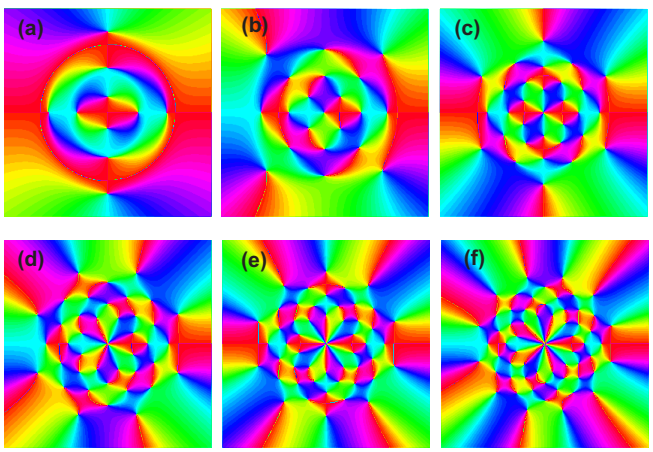

FIG. 9. (Color online) Numerical patterns of the angle function at the far field of the same radial index $p=2$ and different azimuthal index l: (a) $(p,l)=(2,1)$; (b) $(p,l)=(2,2)$; (c) $(p,l)=(2,3)$; (d) $(p,l)=(2,4)$; (e) $(p,l)=(2,5)$; (f) $(p,l)=(2,6)$.

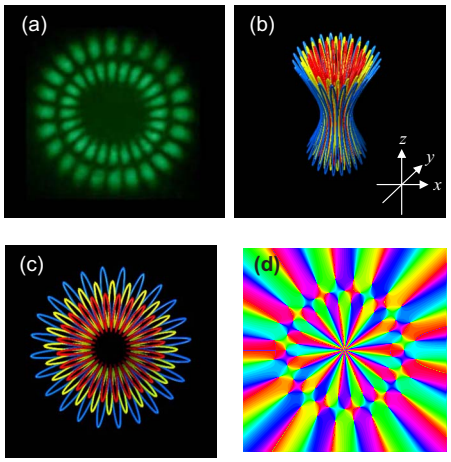

FIG. 10. (Color online) (a) Experimental far-field pattern with radial and azimuthal index $(p,l)=(1,12)$. (b) Structure of C line singularities of the correspondent 3D vector field. (c) Structure of the C line singularities from the view of propagation direction to the beam waist. (d) Numerical pattern of the angle function at the far field.

vector and polarization singularities with the analytical representation of the transverse pattern with the radial and azimuthal index (p,l) to be $(0,4)$ from the view of the propagation direction to the beam waist. The different radial position of the figure implies the different propagation position of the 3D polarization vector field. The minimum of the radial position represents the beam waist and the maximum of the radial position represents the far field. From the analytical structures of the singularities, the polarization state of the experimental 3D vector field under propagation can be clearly revealed. From the loci of C lines, it can be confirmed that L surfaces separate regions of right-handed and left-handed polarization and V points locate on the intersection of right-handed and left-handed polarization.

It is worthwhile to give a more detailed comparison between theory and experimental results. The present hyperboloid structures of polarization singularities are directly derived from Eqs. (2) and (3) in which the two different LG modes are superposed with equal amplitude. For general cases of experimental results, however, the amplitude of the two LG modes can be somewhat different. Nevertheless, with the same theoretical analysis, the distributions of the polarization singularities can be certainly found to be topologically invariant. In other words, the hyperboloid structure of polarization singularities represents a characteristic feature of resonant laser modes emitted from degenerate cavities. On the other hand, more complicated phase singularities, such as link and knot structures, can be produced by using a Gaussian laser beam illuminating a hologram or a phase modulator [30,31]. However, these complex structures are not at all related to the fundamental aspects of laser resonators.

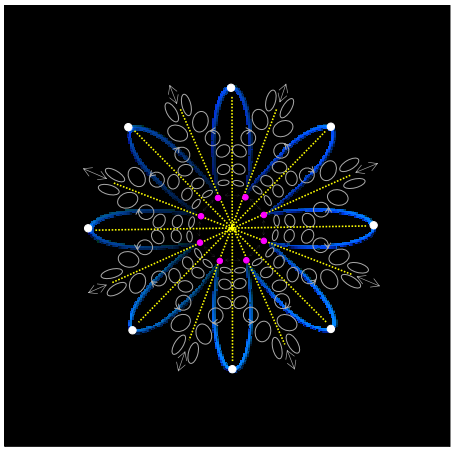

FIG. 11. (Color online) Diagram of the representation of the polarization state under propagation corresponding to the singularities of C lines (blue line), V points (white points at far field and pink points at beam waist), and L surfaces (yellow dashed lines).

The present polarization singularities are explored based on the paraxial approximation in which the longitudinal electric field is neglected. For a rigorous point of view, it is more appropriate to analyze the experimental polarization singularities with the full 3D electric field. Recently, Berry [18] has confirmed that the separations between two singularities obtained with the paraxial approximation and the full 3D fields are generally much smaller than the wavelength. Therefore, the present findings are almost not affected by neglecting the longitudinal field.

IV. CONCLUSION

In conclusion, we have used an isotropic microchip laser to generate the propagation-dependent polarization vector fields with the longitudinal-transverse coupling and the entanglement of the polarization states. It is found that the experimental 3D coherent vector fields can be reconstructed by the orthogonal circularly polarized vortex mode which is made up of two Laguerre-Gaussian (LG) modes with different order. With the analytical representation, the general structures for the singularities of the C lines, V points, and L surfaces can be systematically analyzed. In general, there are $2p+1$ solutions of the radius which the C lines and V points are symmetrically embedded in and the theoretical solutions of the radius can be represented analytically for the cases $p=0-3$. Importantly, the theoretical analyses reveal that the trajectories of the C lines projected on the transverse plane displays the intriguing petal structures. Furthermore, the polarization states of the experimental LG vector fields under propagation can be clearly demonstrated. The generalized structures of the polarization singularities in coherent vector fields may provide some useful insights into the nature of the waves.

[1] M. S. Soskin and M. V. Vasnetsov, Pure Appl. Opt. **7**, 301 (1998).
[2] Michael Berry, Proc. SPIE **4403**, 1 (2001).
[3] J. F. Nye and M. V. Berry, Proc. R. Soc. London, Ser. A **366**, 165 (1974).
[4] G. Blatter, M. V. Feigelman, and V. B. Geshkenbein, Rev. Mod. Phys. **66**, 1125 (1994).
[5] P. Seba, U. Kuhl, M. Barth, and H. J. Stockmann, J. Phys. A **32**, 8225 (1999).
[6] *The Quantum Hall Effect*, 2nd ed. (Springer-Verlag, Berlin, 1990).
[7] M. V. Berry, J. Mod. Opt. **45**, 1845 (1998).
[8] *Optical Vortices*, edited by M. V. Vasnetsov and K. Staliunas (Nova Science, New York, 1999).
[9] M. S. Soskin and M. V. Vasnetsov, in *Progress in Optics*, edited by E. Wolf (Elsevier, New York, 2001), Vol. 42, Chap. 4.
[10] I. Freund, Opt. Commun. **199**, 47 (2001).
[11] L. Gil, Phys. Rev. Lett. **70**, 162 (1993).
[12] T. Erdogan, Appl. Phys. Lett. **60**, 1921 (1992).
[13] Y. F. Chen, K. F. Huang, H. C. Lai, and Y. P. Lan, Phys. Rev. Lett. **90**, 053904 (2003).
[14] I. V. Veshneva, A. I. Konukhov, L. A. Melnikov, and M. V. Ryabinina, J. Opt. B: Quantum Semiclassical Opt. **3**, S209 (2001).
[15] F. Prati, G. Tissoni, M. S. Miguel, and N. B. Abraham, Opt. Commun. **143**, 133 (1997).
[16] T. H. Lu, Y. F. Chen, and K. F. Huang, Phys. Rev. E **75**, 026614 (2007).
[17] J. F. Nye, *Natural Focusing and Fine Structure of Light: Caustics and Wave Dislocations* (Institute of Physics Publishing, Bristol, 1999).
[18] M. V. Berry, J. Opt. A, Pure Appl. Opt. **6**, 475 (2004).
[19] J. F. Nye and J. V. Hajnal, Proc. R. Soc. London, Ser. A **409**, 21 (1987).
[20] I. Freund, Opt. Lett. **29**, 15 (2004).
[21] M. S. Soskin, V. Denisenko, and I. Freund, Opt. Lett. **28**, 1475 (2003).
[22] F. Flossmann, U. T. Schwarz, M. Maier, and M. R. Dennis, Phys. Rev. Lett. **95**, 253901 (2005).
[23] A. Volyar, V. Shvedov, T. Fadeyeva, A. S. Desyatnikov, D. N. Neshev, W. Krolikowski, and Y. S. Kivshar, Opt. Express **14**, 3724 (2006).
[24] M. V. Berry and M. R. Dennis, J. Phys. A **40**, 65 (2007).
[25] Y. F. Chen, T. H. Lu, and K. F. Huang, Phys. Rev. Lett. **97**, 233903 (2006).
[26] Y. F. Chen, T. H. Lu, and K. F. Huang, Phys. Rev. Lett. **96**, 033901 (2006).
[27] Y. F. Chen, T. H. Lu, K. W. Su, and K. F. Huang, Phys. Rev. Lett. **96**, 213902 (2006).
[28] I. Freund, Opt. Commun. **201**, 251 (2002).
[29] G. Indebetouw, J. Mod. Opt. **40**, 73 (1993).
[30] M. V. Berry and M. R. Dennis, Proc. R. Soc. London, Ser. A **457**, 2251 (2001).
[31] J. Leach, M. R. Dennis, J. Courtial, and M. J. Padgett, Nature (London) **432**, 165 (2004).